JOURNAL OF COMPUTATIONAL PHYSICS **126,** 99–108 (1996)
ARTICLE NO. 0123

A New Numerical Algorithm for the Analytic Continuation of Green's Functions

VINCENT D. NATOLI,* MORREL H. COHEN,* AND BENGT FORNBERG†

*Exxon Research and Engineering Company, Annandale, New Jersey 08801 and †University of Colorado, Program in Applied Mathematics, Boulder, Colorado 80309-0526

Received June 2, 1995; revised November 6, 1995

The need to calculate the spectral properties of a Hermitian operator H frequently arises in the technical sciences. A common approach to its solution involves the construction of the Green's function operator $G(z) = [z - H]^{-1}$ in the complex z plane. For example, the energy spectrum and other physical properties of condensed matter systems can often be elegantly and naturally expressed in terms of the Kohn–Sham Green's functions. However, the nonanalyticity of resolvents on the real axis makes them difficult to compute and manipulate. The Herglotz property of a Green's function allows one to calculate it along an arc with a small but finite imaginary part, i.e., $G(x + iy)$, and then to continue it to the real axis to determine quantities of physical interest. In the past, finite-difference techniques have been used for this continuation. We present here a fundamentally new algorithm based on the fast Fourier transform which is both simpler and more effective.

I. INTRODUCTION

The need for the numerical computation of the spectral properties of some Hermitian or symmetric operator $\hat{H}$ is ubiquitous in applied mathematics and the physical and engineering sciences. One powerful and commonly used method is the construction of the resolvent, or Green's function operator,

$$\hat{G} = [z - \hat{H}]^{-1}, \tag{1}$$

where $z = x + iy$ is a variable in a complex eigenvalue plane. Because the eigenvalues of $\hat{H}$ are real, $\hat{G}$ is nonanalytic on the real axis and possesses the Herglotz property; i.e., it can be continued analytically in both the upper and lower open half planes [1]. The eigenvalue spectrum of $\hat{H}$ in the form of the density of states (DOS) is a quantity of central interest. It is given by the trace of the imaginary part of $\hat{G}(z)$ taken in some basis in the limit as z approaches the real axis from above or below. However, in many cases, the DOS is a nonanalytic, or even a singular function of x, and its direct calculation on the real axis is either not feasible or computationally costly. Accordingly, a commonly used approach is to compute the trace of $\hat{G}(z)$ along an arc in the complex plane where it is nonsingular and to continue the result to the real axis. Numerical analytic continuation, however, is notoriously difficult, and most techniques developed thus far are useful only for specific problems.

Hass *et al.* [2] have initiated an approach to such numerical continuation which is often used in condensed matter physics. This procedure has been further refined for electronic structure calculations by Eschrig [3]. Depending on the question to be addressed, a diagonal element, a subtrace, or a trace of $\hat{G}(x, 0^{\pm})$, might be desired [4]. A direct calculation of $G(x, 0^{\pm})$ is computationally very costly because it involves an integral over Dirac-delta functions in reciprocal space,

$$G(x, 0^{\pm}) = \int d^3\mathbf{k} G(\mathbf{k}; x, 0^{\pm}), \tag{2}$$

where $G(\mathbf{k}; x, 0^{\pm})$ is a sum of those diagonal elements of $\hat{G}$ with the same wavevector $\mathbf{k}$, the imaginary part of each of which being a delta function. A very large number of k-points is required to achieve a smooth result. By contrast, the calculation off the real axis, where the delta functions are broadened into Lorentzians, is significantly easier. Computation is therefore carried out along the line $x + iy$ with fixed y. Hass *et al.* then analytically continue $G(z)$ to $G(x, 0^{\pm})$ (+ for $y > 0$ and − for $y < 0$) using a stepwise finite-difference method that makes use of the Cauchy–Riemann relations. Their method has been used extensively on a wide variety of physical systems [5–8] with an accuracy of 5–10%. This is less than the intrinsic accuracy on the order of 1% currently attainable in electronic structure computations. Attempts to increase the precision of the continuation encounter problems either with the instabilities inherent in finite-difference methods or with computation time. Nevertheless, one wants to ensure that ancillary routines like continuation introduce errors smaller than the intrinsic accuracy of the computation at an acceptably low overhead.

In this paper, we present an alternative continuation scheme based on the use of FFTs (fast Fourier transforms). The FFT approach provides a simple, fast, and accurate

0021-9991/96 $18.00

algorithm which has fewer parameters to optimize. In Section II, we discuss the analytical details underlying the new algorithm in the infinite x domain. The FFT algorithm is introduced in Section III. Results are presented in Section IV, and this work is briefly summarized in Section V. Since we are attempting to ''solve''an ill-posed problem numerically, our goal cannot be a perfect reconstruction, but rather to obtain economically the best approximation that appears feasible based on the available data. Additional background to the problem can be found in the excellent reference by Glaser [9]. We have applied the new method successfully to the study of the electronic structure of a pseudomorphic copper overlayer on ruthenium [10].

II. CONTINUATION BY INFINITE-DOMAIN FOURIER TRANSFORMS

A. *The Continuation of $G(z)$ via Fourier Transforms*

The problem, simply stated, is to determine the value of $G(x, 0^{\pm})$ on the real axis given the analytic function $G(z)$ defined along a straight arc with small but finite y, where x represents the real energy E [11]. In the coordinate representation, its explicit form is

$$G(r, r'; z) = \sum_i \frac{\phi_i(r)\phi_i^*(r')}{z - E_i}, \tag{3}$$

where $\phi_i(r)$ is an eigenfunction of $\hat{H}$ with real eigenvalue E_i. In any representation, $G(z)$ has singularities only on the real axis including discrete poles, branch cuts, and even singular continuous spectra. Our goal is to determine $G(x, 0^{\pm})$, where

$$G(x, 0^{\pm}) = \lim_{y \to 0^{\pm}} G(z). \tag{4}$$

The approach is to make a straightforward calculation of $G(z)$ for $|y| \neq 0$, where no difficulty arises from the singularities on the real axis and then to continue to the real axis where $y = 0^{\pm}$.

In what follows, we define the Fourier transform of $G(z)$ along a straight contour and derive an expression which relates $G(x, 0^{\pm})$ to $G(z)$ along a contour of fixed finite y.

Consider the following definition of the Fourier transform pair $G(z)$ and $F(k, y)$,

$$F(k, y) = \int_{-\infty}^{\infty} dx e^{-ikx} G(z) \tag{5}$$

$$G(z) = \frac{1}{2\pi} \int_{-\infty}^{\infty} dk e^{ikx} F(k, y). \tag{6}$$

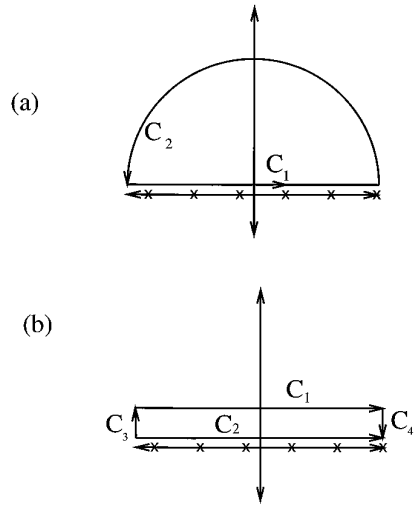

FIG. 1. (a) Contour composed of C_1 and semi-circle C_2 in complex energy space used to evaluate Eq. (7) for $|y| > 0$ and $|k| < 0$. (b) Contour composed of C_1, C_2, C_3, and C_4 in complex energy space used to evaluate Eq. (7) for $|y| > 0$ and $|k| > 0$.

Substituting $z = x + iy$, we may write

$$F(k, y) = e^{-ky} \int_{C_1} dz\, e^{-ikz} G(z). \tag{7}$$

The integration contour C_1 is now the infinite line $z = x + iy$, $-\infty < x < \infty$. To evaluate the contour integral in Eq. (7), consider the four cases that arise from the various possible signs of y and k:

Case i. $y > 0$ and $k < 0$. The arc C_1 may be closed in the upper half plane with the addition of the arc C_2 (see Fig. 1a). The integral around this contour $C = C_1 + C_2$ is zero by Cauchy's theorem since it encloses no singularities, and the integral along C_2 is also zero. The integral along C_1 in Eq.(7) then vanishes.

Case ii. $y > 0$ and $k > 0$. The arc is closed below (see Fig. 1b) by C_2, C_3, and C_4. The contributions from C_3 and C_4 on the left and right ends cancel. Since the contour again contains no singularities, we have

$$\int_{C_1} dz e^{-ikz} G(z) = \int_{C_2} dz e^{-ikz} G(z) \tag{8}$$

$$= \int_{-\infty}^{\infty} dx e^{-ikx} G(x, 0^{+}) \tag{9}$$

$$= F(k, 0^{+}). \tag{10}$$

Case iii. $y < 0$ and $k > 0$. This case is similar to Case i, and the value is also zero.

Case iv. $y < 0$ and $k < 0$. This case is similar to Case ii, and the integral in Eq. (7) is

$$\int_{C_1} dz e^{-ikz} G(z) = \int_{C_2} dz e^{-ikz} G(z) \tag{11}$$

$$= \int_{-\infty}^{\infty} dx e^{-ikx} G(x, 0^-) \tag{12}$$

$$= F(k, 0^-). \tag{13}$$

The expressions (7), (10), and (13) provide a simple relationship between the Fourier transform $F(k, 0^{\pm})$ of $G(x, 0^{\pm})$ and the Fourier transform $F(k, y)$ of $G(z)$. Thus for $y > 0$,

$$\begin{aligned} G(x, 0^+) &= G_1(x, 0^+) - iG_2(x, 0^+) \\ &= \frac{1}{2\pi} \int_0^{\infty} dk\, e^{ikx} e^{ky} F_+(k, |y|) \end{aligned} \tag{14}$$

and for $y < 0$,

$$\begin{aligned} G(x, 0^-) &= G_1(x, 0^-) + iG_2(x, 0^-) \\ &= \frac{1}{2\pi} \int_{-\infty}^{0} dk\, e^{ikx} e^{ky} F_-(k, |y|), \end{aligned} \tag{15}$$

where

$$F_{\pm}(k, |y|) = F_1(k, |y|) \mp iF_2(k, |y|). \tag{16}$$

G_1 and G_2 are the real and imaginary parts of G and $F_{1,2}(k, |y|)$ is the Fourier transform of $G_{1,2}(x, |y|)$ in analogy with Eq. (5). Using the expression $F(k, y) = F^*(-k, -y)$ and the relationship between F_1 and F_2 defined in the Appendix, Eq. (14) and Eq. (15) may be combined to give the central equation of the FFT algorithm,

$$G(x, 0^{\pm}) = \frac{1}{2\pi} \int_{-\infty}^{\infty} dk\, e^{ikx} e^{|k||y|} F_{\pm}(k, |y|). \tag{17}$$

Note the presence of the exponential $e^{|k||y|}$ in the integrand in Eq. (17). This factor displays clearly the ill-posed nature of analytic continuation as it appears in the Fourier transform representation. It shows explicitly how errors in the input data $G(x, |y|^{\pm})$ entering $F(k, |y|)$ are amplified by analytic continuation.

B. *The Nature of the Mapping*

A more detailed analysis of Eq. (17) is presented below to demonstrate and clarify the true nature of the continuation process.

$G(x, 0^{\pm})$ in Eq. (17) must be independent of $|y|$. Thus the class of functions $F(k, |y|)$ for which Eq. (17) holds has an implicit $|y|$ dependence which cancels the factor $e^{|k||y|}$ and a k dependence which leads to convergence of the integral as $k \to \infty$. We can thus replace Eq. (17) by the equivalent form

$$G(x, 0^{\pm}) = \lim_{q \to \infty} \frac{1}{\pi} \int_{-\infty}^{\infty} dk\, e^{ikx} e^{|k||y|} F_{\pm}(k, |y|) e^{-k^2/q^2} \tag{18}$$

containing the convergence factor $\exp[-k^2/q^2]$. This convergence factor allows us to interchange the order of $k-$ and $x'-$ integration after inserting Eq. (5) into Eq. (18). The result is an equation for $G(x, 0^{\pm})$ which illustrates the continuation process as a convolution on $G(x, y)$ with a mapping function $M(x - x', |y|)$,

$$G(x, 0^{\pm}) = \int dx' M(x - x', |y|) G(x', y), \tag{19}$$

where

$$M(x - x', |y|) = \lim_{q \to \infty} \frac{1}{\pi} \int_0^{\infty} dk\, e^{-k^2/q^2} e^{k(|y| + i(x - x'))}. \tag{20}$$

The map M is a distribution as defined by Laurent Schwartz [12] and not a function. By straightforward manipulation, the map M can be put in the form

$$M(x - x', |y|) = \lim_{q \to \infty} \frac{q}{2\sqrt{\pi}} e^{z^2} (2 - \operatorname{Erfc} z) \tag{21}$$

$$z = \frac{1}{2} q(|y| + i(x - x')). \tag{22}$$

Taking the asymptotic limit $|z| \to \infty$ of the Erfc leads to

$$\begin{aligned} M(x - x', |y|) = 2D(x - x', |y|) \\ - \frac{1}{\pi} \frac{|y|}{(x - x')^2 + |y|^2}, \end{aligned} \tag{23}$$

where

$$D(x - x', |y|) = \lim_{q \to \infty} \frac{q}{2\sqrt{\pi}} e^{-\{(1/2)q[(x - x') - i|y|]\}^2}. \tag{24}$$

D in Eq. (24) comprises that part of M which is a distribution. The integral of D over x or x' is unity, but D cannot be regarded as a probability density because it oscillates in sign,

$$D(x - x', |y|) = \lim_{q \to \infty} \frac{q}{2\sqrt{\pi}} e^{-(1/4)q^2[(x - x')^2 - |y|^2]} e^{iq(x - x')|y|/4}. \tag{25}$$

In the limit $q \to \infty$, D vanishes for $|x - x'| > |y|$, oscillates with infinite amplitude and vanishing period for $0 < |x - x'| \leq |y|$, and goes to $+\infty$ at $x = x'$. Thus $D(x - x', |y|)$ has neither values nor derivatives with respect to $x - x'$

in $(-y, y)$. Nevertheless, we are concerned only with its integral properties when Eq. (23) is inserted in Eq. (19).

$G(x', |y|)$ is analytic in x' and possesses a Taylor's series expansion. Thus we need only to establish that all the moments of D exist. We define the moment generating function

$$S(\tau, |y|) = \int dx\, D(x, |y|) e^{-i\tau x} \tag{26}$$

$$= \sum_{n=0}^{\infty} \frac{(-i\tau)^n}{n!} m_n, \tag{27}$$

$$m_n = \int dx\, D(x, |y|) x^n. \tag{28}$$

S is readily evaluated

$$S(\tau, |y|) = \lim_{q\to\infty} \cosh \tau|y| e^{-\tau^2/q^2} \tag{29}$$

$$= \cosh \tau|y|. \tag{30}$$

Comparison of Eq. (30) and Eq. (27) yields the finite moments

$$m_n = 0, \qquad n \text{ odd} \tag{31}$$

$$= (-1)^{n/2}\tau^n, \quad n \text{ even}. \tag{32}$$

Thus convolving $D(x - x', |y|)$ and, therefore, $M(x - x', |y|)$ with any $G(x', |y|)$ yields well-defined results because by definition $G(x', |y|)$ possesses a Taylor series and a Fourier transform.

Because $D(x - x', |y|)$ oscillates infinitely rapidly over a finite interval, in convolving $G(x', |y|)$ with $M(x - x', |y|)$ to obtain $G(x, 0)$ one has effectively constructed $G(x, 0)$ from an infinite set of infinitesimal differences of $G(x', |y|)$ equivalent to an infinite set of derivatives. Since $G(x', |y|)$ is an analytic function which possesses a Taylor's series in x convergent for all x, this constitutes the use of global information on $G(x', |y|)$ in constructing $G(x, 0)$. It is this use of global information which is the basis of the improvement of accuracy of the FFT method described in the next section. This is in contrast to the step-wise finite difference methods which use only local information.

The arguments used to obtain the mapping $M(x - x', |y|)$ carrying $G(x, |y|)$ into $G(x, 0)$ could equally well have been used to construct the inverse mapping

$$G(x, |y|) = \int dx'\, M^{-1}(x - x', |y|) G(x, 0) \tag{33}$$

with the result that it is a function, not a distribution,

$$M^{-1}(x - x', |y|) = \frac{1}{\pi} \frac{|y|}{(x - x')^2 + |y|^2}. \tag{34}$$

We thus see that $M(x - x', |y|)$ given by Eq. (23) and Eq. (24) is the inverse of the Lorentzian Eq. (34), a remarkable result which holds, however, only within the manifold of functions possessing the same analytic properties as $G(z)$. In the general case, the Lorentzian map has no inverse; in the present case it does, and the inverse is a distribution of singular richness.

III. FAST FOURIER TRANSFORMS

Up to this point we have derived analytic expressions which are valid over the whole range of real x. As a practical matter, the Fourier transform is most easily and efficiently accomplished on a discrete bounded grid through the use of the FFT. Replacing the integrals in Eq. (17) by sums on a discrete mesh we have

$$G(x, 0^{\pm}) = \frac{1}{2\pi} FFT^{-1}[e^{|k||y|} FFT[G(x', y)]]. \tag{35}$$

The use of Eq. (35) to continue a typical function results in instabilities that manifest themselves as oscillations near the most singular parts of the function and at the endpoints. The source of these oscillations and a scheme for their elimination emerges from a study of the various error sources introduced by the FFT. These error sources and the techniques to minimize them are discussed in the following subsections.

A. *Error Estimation*

There are four main sources of error introduced by the use of FFTs. The first and second are the errors introduced by replacing a continuous integral by a discrete sum for both x and k. The third and fourth error sources are due to the terms neglected when the two integrals are truncated by the FFT.

Discretization of the integral of a function $f(x)$ over a finite interval using the rectangular rule results in the error,

$$\varepsilon = \frac{L}{24} \Delta_x^2 \overline{f_n''}. \tag{36}$$

Here Δ_x is the mesh spacing and f_n'' is the second derivative of the integrand f at the point n. In the case of Eq. (17) we have an integral on k over $F(k, y)$ and the implied integral (5) on x over $G(z)$ to get $F(k, y)$. We designate T_1 as the error due to the discretization of integral (5). Then f_n is $e^{-ikn\Delta_x} G(n\Delta_x, |y|)$, and Eq. (36) demonstrates that the discretization error, T_1 scales as Δ_x^2. The finer the mesh the more accurate the result, as one might expect. For the integral on k in Eq. (17), f_m is $e^{i(\pi m/L)x} e^{|2\pi m/L||y|} F_{\pm}(2\pi m/L, |y|)$, and the error, which we denote as T_2, scales as $\Delta_k^2 = (2\pi/L)^2$. Thus as expected increasing the interval

length L and decreasing the distance between mesh points increases the overall accuracy by reducing the error terms T_1 and T_2.

It is critical to note, however, that the upper bound on the k integral, T_2, is π/Δ_x, which increases as Δ_x decreases. A problem arises in that errors incurred in the calculation of $F(k, |y|)$ are multiplied by the exponential $e^{|k||y|}$ and will overwhelm the sum at large k. Thus there exists some optimal relationship between y and Δ_x which may be estimated by considering the overall dependence of T_1 on Δ_x. The error T_1 in $F(k, |y|)$ scales like a constant multiplied by Δ_x^2 and by the sum in Eq. (36). The highest k is π/Δ_x, and thus the contribution to T_1 of the most troublesome term in the k integral is $Ce^{(2\pi/\Delta_x)|y|}\,\Delta_x^2$. Differentiating with respect to Δ_x, we find the minimum at $\Delta_x \approx \pi|y|$. This qualitative argument predicts that, for simplicity and good results, Δ_x should be set roughly equal to $|y|$. Another way to see that the optimal value of Δ_x is approximately y is to recognize that $M^{-1}(x - x', |y|)$ smears all singularities over a half width of order $|y|$. There is thus no need to sample x more closely, a result confirmed by a numerical study. The contribution to this error term T_1 in the k sum is then $Ce^2(\pi|y|)^2$ and is reduced by decreasing $|y|$. However, there is a limit to how small one can take $|y|$ because of those difficulties which arise in the calculation of $G(z)$ which motivated the continuation approach to calculating $G(x, 0)$ in the first place. Smaller $|y|$ means a more complex and costly calculation of $G(z)$, so that the value of $|y|$ is set by considerations of computer time.

The truncation error is that contribution to $G(x, 0)$ which comes from the neglected wings of $G(x, y)$. The mapping function $M(x - x'; y)$ makes it clear that only the Lorentzian term will be important here since D is only nonzero for $|x - x'| < y$ and y is approximately Δ_x. Thus, even though the Lorentzian dies off rapidly, it does yield a finite contribution from the wings which is neglected by the FFT. This error may be estimated by considering the isolated singularity at $z = 0$, given by $G(z) = 1/z$. Using Eq. (19) we may write an expression for the contribution to $G(z)$ from the neglected wings,

$$T_3 = \left(\int_{-\infty}^{-L/2} + \int_{L/2}^{\infty}\right) dx'\, M(x - x', y)\,\frac{y}{x'^2 + y^2}. \quad (37)$$

Noting that $x'^2 \gg y^2$, the integral simplifies to

$$T_3 = -\frac{1}{\pi}\,\mathrm{Im}\left[\frac{2}{L(x + iy)} + \frac{1}{(x + iy)^2}\ln\left(\frac{L/2 - x - iy}{L/2}\right)\right]. \quad (38)$$

Using Eq. (38), we find that for typical values of L and y, this error is a number on the order of 10^{-5}. The contribution to the error from truncation is therefore small enough to be ignored.

The k integral also contributes an error term, T_4, due to truncation that is

$$T_4 = \int_{\pi/\Delta_x}^{\infty} dx\, e^{ikx}e^{|k||y|}F(k, |y|) + \int_{-\infty}^{-\pi/\Delta_x} dk\, e^{ikx}e^{|k||y|}F(k, |y|) \quad (39)$$

which decreases with decreasing Δ_x. The most serious consequence associated with this truncation is the introduction of the Gibbs phenomenon at the end points and singular points on x. By not including the highest k values in the sum, contributions from the k near the cutoff are insufficiently cancelled and result in spiked or oscillatory features. Such errors can be substantially reduced by filtering as described in Subsection III B below.

This analysis of the contributions to the error reveals that Δ_x should be chosen approximately equal to y in order to minimize the error from T_1 and T_4 and yet avoid error and instability from the exponential factor present in T_2, while $|y|$ should be taken as small as possible subject to limitations on computation time.

B. *Error Reduction through Filtering*

The terms T_1 and T_4 are minimized by taking Δ_x as small as possible, but, as discussed in Section III A, there is a limit to how small Δ_x can be. This limit exists because of small errors in the calculation of $F(k, |y|)$ which prevent it from cancelling the $e^{|k||y|}$ term in Eq. (17). According to Eq. (7) and Eq. (10), $F(k, |y|)$ depends on $|y|$ only through the factor $e^{-|k||y|}$. Thus, if the numerical computation of $F(k, |y|)$ were precise, the dangerous factor $e^{|k||y|}$ in Eq. (17) would be completely cancelled. Computational errors in $F(k, |y|)$ prevent perfect cancellation and leads to an error that diverges exponentially with increasing k. In addition, the truncation of the k integral causes an incomplete cancellation of terms that results in the Gibbs phenomenon.

To reduce magnified errors from terms at high $|k|$ which would contribute little if calculated exactly and to alleviate the effects of truncation errors, a filtering factor is used which damps the highest $|k|$ contributions. Equation (35) is modified as follows to include this factor:

$$G(x, 0) = \frac{1}{2\pi}\,FFT^{-1}[e^{-k^2/k_0^2}e^{|k||y|}FFT[G(x', |y|)]]. \quad (40)$$

This Gaussian filter improves the stability and accuracy of the FFT algorithm and ameliorates the Gibbs phenomenon. A more general form such as $\exp[-(k/k_0)^n]$ was investigated, but numerical studies show that little is gained by

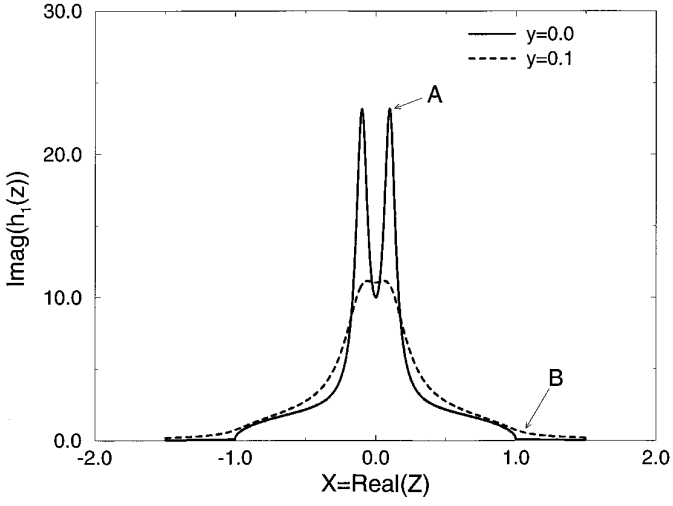

FIG. 2. Imaginary part of h_1 plotted for $-2 < x < 2$ and $y = 0^+$ (solid line), $y = 0.1$ (dotted line).

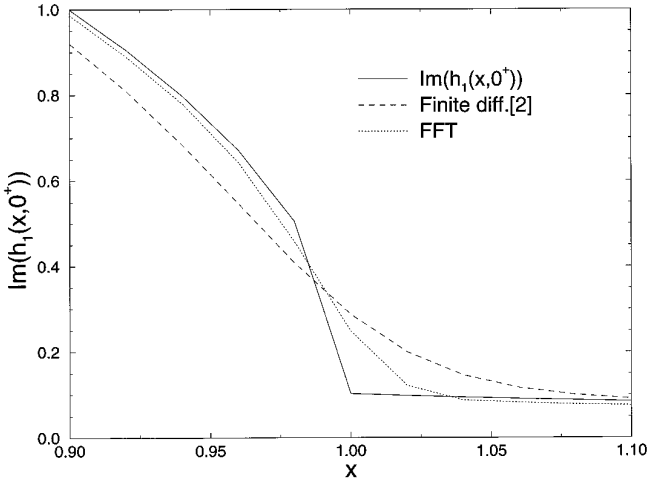

FIG. 4. Comparison of old and new continuation with true analytic function $h_1(x, 0^+)$ at point B of Fig. 2.

taking n different from 2. For $n = 2$, we find $k_0 \approx \pi/(2\Delta_x)$ to be optimum.

IV. RESULTS

A. *Comparison with Finite Difference Methods: Analytic Test Functions*

We now summarize and compare the properties of the proposed FFT approach and the finite difference method. Both are linear functionals scaling with computational complexity $O(N)$ and $O(N)\mathrm{Log}(N)$ for finite-difference and FFT, respectively. The FFT uses all the available data and consequently yields a more accurate continuation. We find the effective prefactor for the FFT method including the $\mathrm{Log}(N)$ term to be about five times that of the finite-difference approach for typical problems. Nevertheless the time spent on either continuation is negligible because the bulk of the effort is expended on the calculation of $G(z)$ along an arc in the complex plane. Our goal therefore has been to find the most faithful method of continuation given a fixed number of evaluation points along an arc in the complex plane. Computer time required for the continuation was not an issue as long as it remained much less than the time to evaluate $G(z)$. We shall consider two sample functions with which we demonstrate the accuracy of the proposed continuation algorithm and make comparison with the finite difference method. The first function we consider is the severe test function used by Hass *et al.* in Ref [2]. The function,

$$h_1(z) = 2(z - \sqrt{z^2 - 1}) + \frac{1}{z + 0.1 + 0.05i} + \frac{1}{z - 0.1 + 0.05i} \tag{41}$$

is analytic in the upper half plane with singularities at $z = \pm 0.1 - 0.05i$. While not meromorphic, it exhibits many of the same properties as a physical Greens function. Following the procedure in Ref. [2], we evaluate $h_1(z)$ at $y = 0.1$ and continue to the real axis. We use an energy spacing $\Delta E = 0.02$ and we set $M = 5$ for the finite difference algorithm exactly as in [2]. In the terminology of Ref. [2], M designates the number of steps to the real axis. Figure 2 shows the function along $z = x + 0.1i$ and on the real axis, where $y = 0^+$, over a range $-2 < x < 2$. The continuation

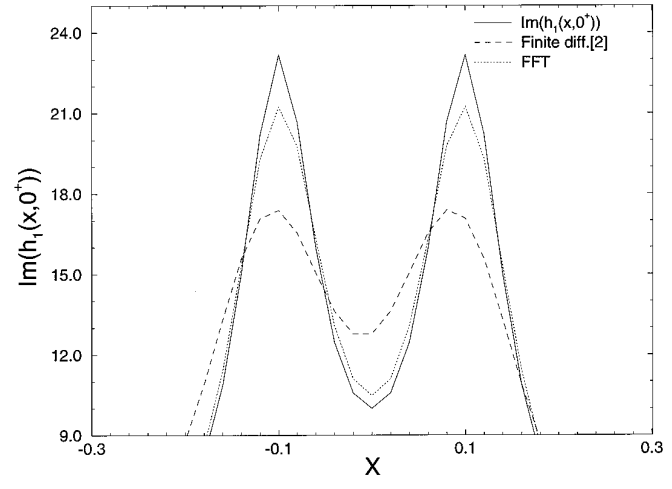

FIG. 3. Comparison of old and new continuation with true analytic function $h_1(z)$ at point A of Fig. 2. The solid line is the same as for Fig. 2 but with an expanded x scale.

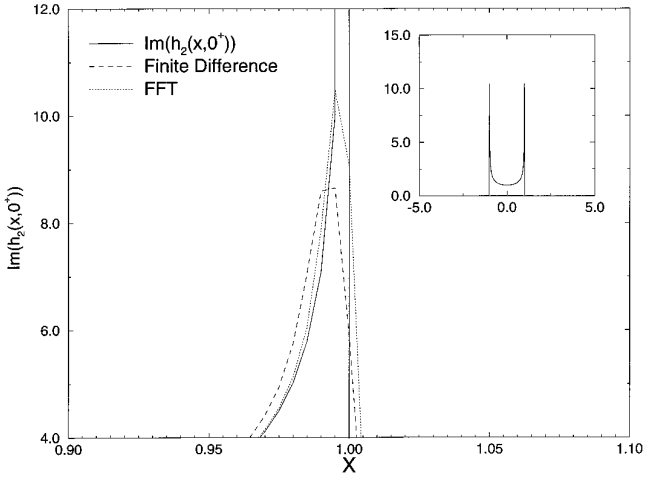

FIG. 5. Comparison of old and new continuations with analytic function $h_2(z)$ near the singularity at $x = 1$. Inset shows $h_2(x)$ plotted over the range $-5 < x < 5$.

procedure is most challenged at the points labeled A and B. These sharp features near the real axis in $h_1(z)$ are representative of the types of singularities one might see in the physical Greens function. The accurate representation of these peaks is necessary in cases where high resolution is required for interpretation [10]. Figures 3 and 4 provide a direct comparison of the old and new algorithms at points A and B along with the true analytic function. Figure 3 shows the dramatic improvement which is possible using the new algorithm. The error in the representation of the peak at A with the finite difference algorithm is 25% while that with the new algorithm is 8%. In Fig. 4, a similar accuracy is demonstrated at point B at a sharp discontinuity in slope where the contribution from the square root term ends.

The second function we present is the density of states one calculates for a simple cosine band, a still more severe test,

$$h_2(z) = \frac{1}{\sqrt{z^2 - 1}}. \tag{42}$$

The function has singularities on the real axis at $x = \pm 1$. We continue $h_2(z)$ from $y = 0.01$ to the real axis and use $\Delta E = 0.01$. We use $M = 5$ as before in the finite difference approach. In Fig. 5 we show the results for the whole range $-5 < x < 5$ in the inset graph while the main plot compares the old and new continuations near the singularity point $x = +1$. We see that the new approach more closely models the true singularity for $x < 1$, where $\mathrm{Im}\, h_2(x, 0^{\pm})$ is nonzero. However, it is somewhat worse for $x > 1$, where $\mathrm{Im}\, h_2(x, 0^{\pm})$ vanishes. One expects large errors at the singularities where the analytic function has infinite value, a severe test for both methods.

B. *Comparison with Finite Difference Methods: Bulk DOS for Fcc Silver*

In addition to the comparison using analytic functions, we demonstrate the effectiveness of the FFT algorithm for a real calculation of the bulk DOS of silver. The tight-binding linear-muffin-tin orbital (TB-LMTO) [13] method is used with the local density approximation (LDA) to solve the Kohn–Sham density-functional equations self-consistently. Within this approach an expression is available for the trace of the Kohn–Sham Green's function $G(z)$. We define the quantity

$$N(E, y) = \frac{1}{\pi} \mathrm{Im\ Tr}\, G(E - iy), \quad y > 0. \tag{43}$$

We calculate $N(E, y)$ by the decimation technique [14]. The calculation becomes increasingly costly as y decreases. Figure 6 illustrates the convergence of $N(E, y)$ along three different lines above the real axis: (a) $y = 0.0001$; (b) $y = 0.002$; and (c) $y = 0.01$ with an increasing number of k vectors, the number of points in reciprocal space used for the numerical integration of Eq. (2). It is clear that convergence becomes significantly more difficult as the real axis is approached. At $y = 0.01$ convergence is reached for 55 k vectors, while at $y = 0.002$, 820 are required, and at $y = 0.0001$ even 20100 are not sufficient. The energy spacing for these calculations is 0.001 Ry, and the longest calculation requiring 20100 vectors took 111 h on an SGI Challenger. For a given value of y, computing time scales linearly with the number of reciprocal vectors included.

The following comparison was made of the efficacy of the FFT and the finite difference algorithms. A relatively quick calculation of $N(E, y)$ was done at $y = 0.01$ and then continued to $y = 0.002$. The results are compared in Fig. 7 along with a direct (not continued) calculation at $y = 0.002$, which took considerably longer. The energy spacing was 0.005 Ry for the two continued calculations and 0.001 Ry for the direct result. The figure demonstrates that the FFT algorithm tracks the exact result much more closely. The detail in the peaks is markedly improved over the finite difference result. In the tail region below about -0.625 Ry, the FFT result tracks the exact result much more closely and is virtually indistinguishable in the region below -0.675 Ry. The three major peaks at -0.61 Ry, -0.51 Ry, and -0.39 Ry are each more accurately depicted in height and width and centroid by the FFT approach. In fact, the shapes of all major peaks are accurately reproduced except at those points which lie between the points at which the FFT was evaluated. One drawback of the finite difference algorithm is that it tends to shift peaks as a result of subtraction and step-wise continuation. This is apparent in each of the three major peaks. Other details are also more clearly represented by the FFT algorithm.

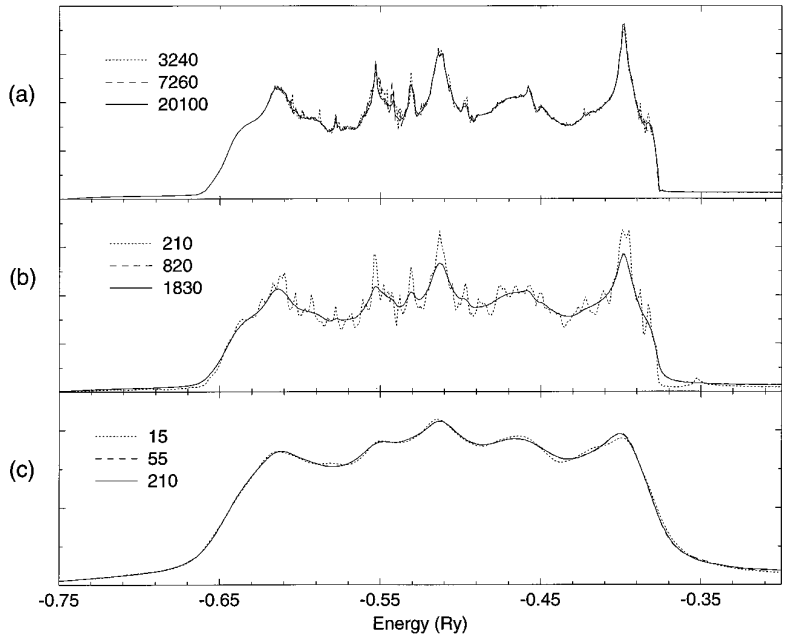

FIG. 6. $N(E, y)$ for fcc silver calculated along three different straight contours displaced from the real axis: (a) $y = 0.00001$; (b) $y = 0.002$; (c) $y = 0.01$. The numbers in the legend refer to the number of reciprocal lattice vectors used in the calculation.

For example the subtle shoulders at -0.59 Ry, -0.54 Ry, and -0.42 Ry are all captured by the FFT routine but missed by the finite-difference approach. In addition, the peak at -0.53 Ry and the asymmetry in the peak at -0.46 Ry are both at least hinted at in the FFT results, but are completely absent in the results for the finite-difference approach.

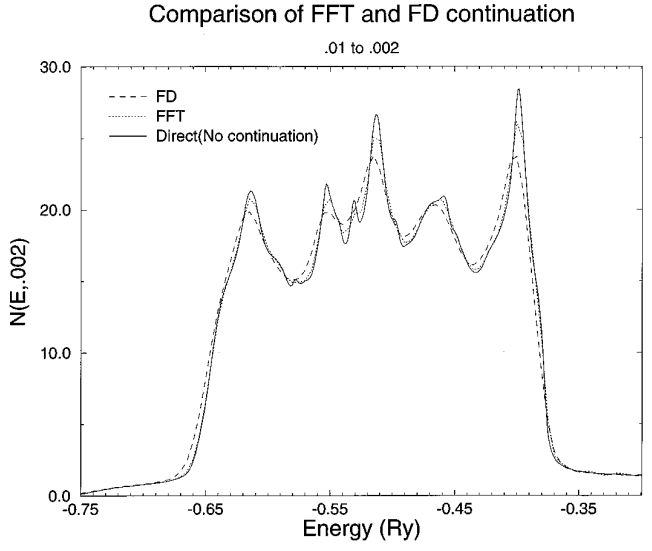

FIG. 7. A comparison of the finite difference and FFT continuation algorithms with the direct calculation using 1830 reciprocal lattice vectors. The continuation is made from $y = 0.01$ to $y = 0.002$ of the imaginary part of the trace of the Greens function for fcc silver.

In Fig. 8, the continuation is made from $y = 0.1$ to $y = 0.00001$, which for practical purposes is the real axis. The jagged oscillations which are most obvious in the energy range between -0.59 Ry and -0.62 Ry indicate that the direct calculation, which used 20100 reciprocal space vectors, is still incompletely converged. As expected the peaks have narrowed, and the features have become sharper in comparison with the direct calculation at $y = 0.002$. In particular, the peaks at -0.55 Ry and -0.39 Ry have become extremely narrow, and the asymmetry at -0.46 Ry is much more pronounced. Since the continuations for both the FFT and finite difference methods are produced on a grid with energy spacing 0.005 Ry, it cannot resolve features with width less than this amount. For example, the very sharp peak at -0.55 Ry is missing from both the continued results because its width is 0.0025 Ry. In general, however, it is clear that the FFT routine tracks the direct result much more closely. It captures all features which have a scale larger than the spacing of the grid and may therefore be considered resolution-limited. As a final quantitative comparison of errors, Fig. 9 compares the rms error in the DOS using the direct calculation as the standard. For each y displacement from the real axis shown, a continuation is made using both the finite difference and FFT methods and the rms error is calculated. In each case, the FFT result is significantly better. The improvement ranges from 35% at $y = 0.0001$ to 28% at $y = 0.008$.

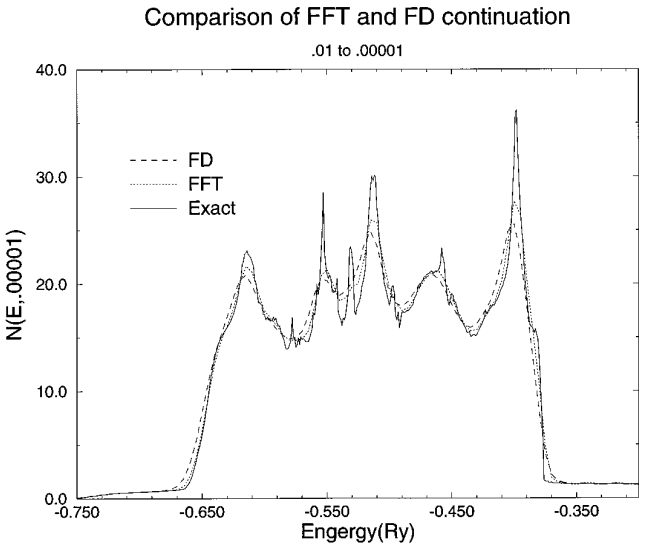

FIG. 8. A comparison of the finite difference and FFT continuation algorithms with the direct calculation using 20100 reciprocal lattice vectors. The continuation is made from $y = 0.01$ to $y = 0.00001$ of the imaginary part of the trace of the Greens function for fcc silver. In the limit as $y \to 0$, the ordinate $N(E, y)$ approaches the DOS per atom of bulk fcc silver.

V. DISCUSSION AND CONCLUSION

In conclusion, we have demonstrated a new algorithm based on FFTs for the continuation of Greens functions. Its implementation is extremely simple and results are improved over the finite difference approach that is currently used. In addition, we show that the continuation procedure can be represented as a convolution with a mapping function M, defined in Eq. (20) which contains contributions from a distribution D and a Lorentzian. We show that optimal results are obtained when the distance to the real axis, y, is comparable to the spacing of energy points on the axis and that instabilities will result when the spacing is taken much smaller than y.

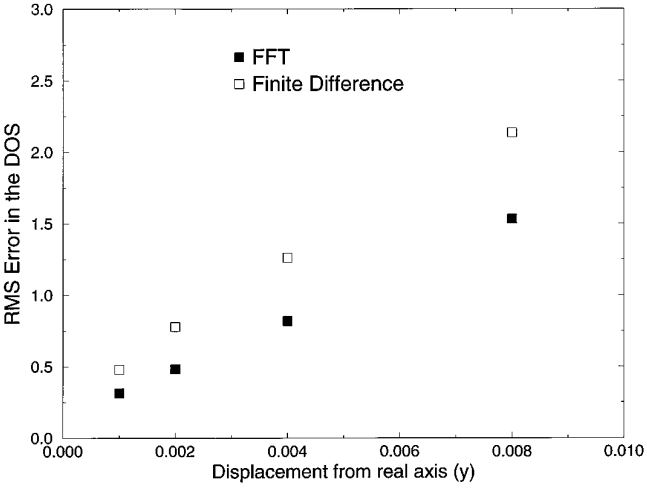

FIG. 9. Comparison of the rms error in the DOS for the FFT and finite difference algorithms. The x-axis shows the starting displacement for the continuation to the real axis.

APPENDIX A: EXPRESSION OF F_1 IN TERMS OF F_2

We can express $G(z)$ as

$$G(z) = \frac{1}{2\pi}\int_{-\infty}^{\infty} dk\, e^{ikx}e^{-ky}\, F(k, 0^{\pm}), \tag{A1}$$

where $\pm = \operatorname{sgn} y$. The Green's function vanishes asymptotically as $1/z$ for a bounded spectrum, Eq. (1). That fact and the analyticity of G off the real axis force $F(k, 0^+)$ to vanish for $k < 0$ and $F(k, 0^-)$ to vanish for $k > 0$ and similarly for $F(k, y)$. We define the real and imaginary parts of $F(k, y)$,

$$F(k, y) = a(k) + ib(k), \tag{A2}$$

where both $a(k)$ and $b(k)$ are real.

The real and imaginary parts of $G(z)$ for $y > 0$ are

$$G_1(z) = \frac{1}{2\pi}\int_0^{\infty} dk\, \{a(k)\cos(kx) - b(k)\sin(kx)\}. \tag{A3}$$

$$G_2(z) = \frac{1}{2\pi}\int_0^{\infty} dk\, \{a(k)\sin(kx) + b(k)\cos(kx)\}. \tag{A4}$$

The Fourier transforms of $G_1(z)$ and $G_2(z)$ are defined as $F_1(k, y)$ and $F_2(k, y)$, respectively, so that

$$F_1(k, y) = \frac{1}{2\pi}\int_{-\infty}^{\infty} dx \int_0^{\infty} dk'\, \{a(k')\cos(k'x) - b(k')\sin(k'x)\}e^{-ikx} \tag{A5}$$

$$F_2(k, y) = \frac{1}{2\pi}\int_{-\infty}^{\infty} dx \int_0^{\infty} dk'\, \{a(k')\sin(k'x) + b(k')\cos(k'x)\}e^{-ikx}. \tag{A6}$$

Expanding the cosine and sine expressions in terms of exponentials leads to

$$F_1(k, y) = \frac{a(k)}{2} - \operatorname{sgn} k\, \frac{b(k)}{2i} \tag{A7}$$

$$F_2(k, y) = \frac{b(k)}{2} + \operatorname{sgn} k\, \frac{a(k)}{2i}. \tag{A8}$$

Thus,

$$F_1(k, y) = +i \operatorname{sgn} k \, F_2(k, y) = -i \operatorname{sgn} k \, F_2(k, |y|) \quad \text{(A9)}$$

and the analogous expression for $y < 0$ is

$$F_1(k, y) = -i \operatorname{sgn} k \, F_2(k, y) = -i \operatorname{sgn} k \, F_2(k, |y|). \quad \text{(A10)}$$

ACKNOWLEDGMENTS

We acknowledge helpful conversations with J. Kudrnovský and M. V. Ganduglia-Pirovano.

REFERENCES

1. P. Singh and W. J. Thompson, *Comput. Phys.* **7**(4), 388 (1993).
2. K. C. Hass, B. Velicky, and H. Ehrenreich, *Phys. Rev. B* **29,** 3697 (1984).
3. H. Eschrig, R. Richter, and B. Velicky, *J. Phys. C: Solid State Phys.* **19,** 7173 (1986).
4. In the following, the symbol $\hat{G}$ is used throughout for the abstract operator and the symbol G is used for one or a collection of its matrix elements in any convenient representation.
5. J. Kudrnovský, B. Wenzien, and V. Drchal, *Phys. Rev. B* **44,** 4068 (1991).
6. J. Kudrnovský, I. Turek, V. Drchal, P. Weinberger, N. E. Christensen, and S. K. Bose, *Phys. Rev. B* **46,** 4222 (1992).
7. M. V. Ganduglia-Pirovano, J. Kudrnovský, I. Turek, V. Drchal, and M. H. Cohen, *Phys. Rev. B* **48,** 1870 (1993).
8. M. H. Cohen, M. V. Ganduglia-Pirovano, and J. Kudrnovský, *Phys. Rev. Lett.* **72,** 3222 (1994).
9. U. H. Glaser, P. Rennert, J. Masek, and B. Velicky, *Phys. Status Solidi B* **134,** 659 (1986).
10. V. Natoli, M. H. Cohen, M. V. Ganduglia-Pirovano, J. Kudrnovský, I. Turek, and V. Drchal, *Surface Sci.* **331,** 716 (1995).
11. The derivations presented in this section are described in many other sources. A particularly good reference is P. Morse and H. Feshbach, *Methods of Theoretical Physics Part I* (McGraw–Hill, New York, 1953).
12. M. J. Lighthill, *Introduction to Fourier analysis and Generalized Functions* (Uni. Press, Cambridge, 1958).
13. O. K. Andersen and O. Jepsen, *Phys. Rev. Lett.* **53,** 2571 (1984).
14. M. P. Sancho, J. M. Lopez Sancho, and J. Rubio, *J. Phys. F* **15,** 851 (1985).